Available online at www.sciencedirect.com
SCIENCE DIRECT
Planetary and Space Science 54 (2006) 528–540
Planetary and Space Science
www.elsevier.com/locate/pss

Ground-based GPS imaging of ionospheric post-seismic signal

Philippe Lognonné[a,*], Juliette Artru[b], Raphael Garcia[a], François Crespon[a], Vesna Ducic[a], Eric Jeansou[c], Giovani Occhipinti[a], Jérôme Helbert[c], Guilhelm Moreaux[c], Pierre-Emmanuel Godet[a]

[a]*Laboratoire d'Etudes Spatiales et de Planétologie, Institut de Physique du Globe de Paris, UMR7154, 4 Avenue de Neptune, 94100 Saint Maur des Fossés Cedex, France*
[b]*Seismological Laboratory, California Institut of Technology, Pasadena, CA, USA*
[c]*NOVELTIS, Parc Technologique du Canal, 2 Avenue de l'Europe, 31520 Ramonville, Saint Agne, France*

Received 1 March 2005; received in revised form 27 July 2005; accepted 14 October 2005

Abstract

During the Demeter mission, a continuous global positioning system (GPS) ionospheric tomography above Europe, Japan and California will be performed with the Service and Products of ionosphere Electronic Content and Tropospheric Refractive index over Europe (SPECTRE) experiment. The main goal of the conducted observations is to detect and characterize post-seimic ionospheric perturbations associated to seismic generated waves, more precisely near field seismic waves, far field Rayleigh waves and tsunamis. We first review the theory describing post-seismic ionospheric signals as well as the most recent observations of these signals. We then present the description of the tomographic procedure used for the SPECTRE experiment, as well as the obtained tomographic models. We finally draw the perspective of such observations.

Keywords: Surface waves; Tsunamis; TEC; Global positioning system; Remote sensing

1. Introduction

Recent developments in ionosphere remote sensing, in particular techniques using the global positioning system (GPS) provide an unprecedented capability for monitoring the state of the ionosphere, its reaction to solar events as well as ionospheric wave phenomena. But the ionosphere is also an important Earth layer for solid Earth geophysicists. The structure and activity of the ionosphere is indeed not only related to solar–terrestrial interactions, but also to solid Earth-atmosphere. Three types of signals can be addressed by a routine survey and monitoring of the ionosphere. The first ones are produced by an acoustic coupling between the solid Earth and the ionosphere and lead to post-seismic signals or alternatively, to signals related to atmospheric explosion, either from volcanoes or asteroids or from anthropogenic origin. The second are related to coupling of oceanic gravity waves (i.e. tsunami) with atmospheric and ionospheric gravity waves. The third ones are related to electromagnetic coupling between the solid Earth and the ionosphere and might be observed either during or after quakes, but also possibly before earthquakes. For a general review of both signals, see Parrot et al. (1993).

While the main objective of the Demeter mission is related to the pre-seismic electromagnetic signals, this paper and the associated investigations are mainly related to the post-seismic signals and only a short review of the observations of pre-seismic total electronic content (TEC) anomalies is provided. Post-seismic ionospheric signals are associated to the waves generated by earthquakes. The possible signals are therefore due to near-field post-seismic, to the far-field Rayleigh waves and to trans-oceanic or near field tsunami waves. For these waves, the ionosphere is acting as a natural amplifier of ground measurements and the vertical velocity at the ground level being amplified by a factor up to 10^5 when it reaches the ionosphere. This

*Corresponding author. Tel.: +33 145114251; fax: +33 145114257.
E-mail address: lognonne@ipgp.jussieu.fr (P. Lognonné).

0032-0633/$ - see front matter © 2006 Elsevier Ltd. All rights reserved.
doi:10.1016/j.pss.2005.10.021

amplification, resulting from the conservation of kinetic energy as the atmospheric density decreases, can be used for detecting, monitoring, and characterising ionosphere perturbations related to geophysical processes on a routine basis.

2. Previous observations and theories

After an earthquake, seismic waves impose vertical and horizontal motion of the surface of a planet. By continuity of the vertical displacement, the atmosphere is forced to move with a vertical velocity equal to the surface vertical velocity, and within favorable wavelength and frequency ranges, the perturbation induced propagates upward as an atmospheric wave. These atmospheric vibrations produce adiabatic pressure and temperature variations up to the ionosphere, as shown in Fig. 1.

The first published observations were performed with ionospheric sounders after the great Alaska earthquake in 1964 (Bolt, 1964; Davies and Baker, 1965). More observations were later reported by Yuen et al. (1969), Weaver et al. (1970) and Blanc (1985). These early observations were performed for very large earthquakes with magnitude greater than $M_s = 8$ and are corresponding to the vertical oscillations of the ionosphere, which is indeed measured directly by the sounder. The development of Doppler sounders in the last 13 years has lead to a reduction of the detection threshold. Modern sounders, such as the Doppler sounder operated by CEA/DASE in France and working continuously since August 1999, are detecting most of the earthquakes with $M_s > 6.5$ (Artru et al., 2004). Doppler data are very similar to seismograms in the sense that they measure directly the vertical motion of a given ionospheric layer. However, they remain limited to a small number of point measurements and cannot resolve the 3D structure of the perturbation.

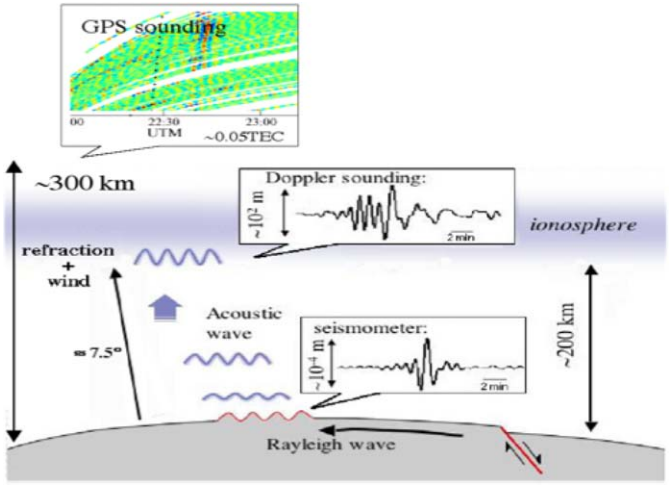

Fig. 1. Examples of observations for ionospheric seismic signals. Observation at altitude of 150–200 km are performed with High Frequency Doppler sounder for earthquakes of magnitude greater than 6.5 whereas observations at higher altitude, performed by GPS networks, can be done only for large quakes with $M_s > 8$ (after Ducic et al., 2003).

The GPS, with the development of the associated ground networks, has opened new possibilities in the detection and imaging of these signals. As a by-product of geodetic measurements, phase and code measurements from GPS stations can be used to calculate the electron density of the ionosphere between the receiver and the satellite. The primary data provide the integrated value of the electron density, or TEC (e.g. Mannucci et al., 1998). The development of dense continuous networks provides therefore unique opportunities to perform dense measurements, leading to a 2D or 3D characterization of transient ionospheric signals. For that reason, GPS have been used to detect traveling ionospheric disturbances (TIDs) (e.g. Afraimovich et al., 1998; Calais et al., 2003), acoustic shock waves generated by rockets or mine blast (Li et al., 1994; Calais and Minster, 1996; Calais et al., 1998a, b, Afraimovich et al., 2001a), ionospheric perturbation associated to solar eclipses (Tsai and Liu, 1999) and seismic signals. The first seismic observations were performed by Calais and Minster (1995), who detected perturbations in the ionospheric total electron content above Southern California after the 1994 Northridge earthquake ($M_s = 6.7$). Afraimovich et al. (2001b) have then considered the problem of interpreting TEC measurements for detection purposes. They have studied GPS-based measurements of TEC to determine parameters of acoustic shock waves associated with two earthquakes that occurred in Turkey in 1999. They measured TEC perturbations following the earthquakes and were able to infer source parameters in remarkable agreement with seismic measurements. A next step was performed by Ducic et al. (2003) following the 2002 Denali earthquake ($M_s = 7.9$). The dense California GPS networks was used to map the ionospheric perturbations and to compute the group velocity of surface waves with a high spatial resolution above the Northwestern US coast, with a precision compatible with the identification of the signature associated to lateral variation in the Earth's lithosphere. The 3D structure of the Denali ionospheric signal was then characterized by Garcia et al. (2005) and with such approach, the comparison of signals from identical altitude can be performed.

The first theories developed to explain these signals have not considered the coupling between the solid Earth and the atmosphere/ionosphere system and were based on the physics of acoustic-gravity waves (Hines, 1960). They assumed that the seismic deformations of the Earth surface were acting as a source generating atmospheric signals and that no energy in the atmosphere was coming back to the Earth interior. Such theories were used by Wolcott et al. (1984) for explaining Doppler data and by Davies and Archambeau (1998), who developed a direct modeling of these waves for a simple representation of shallow seismic sources, including high-frequency components of the wave-packet and nonlinear effects. A more detailed theory was then developed by Lognonné et al. (1998) to take into

account the coupling between the solid Earth, the ocean and the atmosphere. In the later, the boundary conditions of the elasto-dynamic operator at the solid Earth-atmosphere interface is integrated in the normal modes theory. A radiative boundary condition is implemented at the top of the atmosphere, in order to simulate the escape of acoustic and gravity atmospheric waves in the upper ionosphere, where no refraction of waves is observed. This theory allows the computation of normal modes, and those can be used to compute not only seismograms for spherical models, but also barograms and Doppler ionograms. Artru et al. (2001) have later incorporated the dissipation related to viscosity and validated the simulation with Doppler sounding data (Artru et al., 2004). This technique provides the neutral density perturbation and velocities of the upper atmosphere. From this, the electronic density perturbation can be estimated.

A closer examination of the phenomena can be done by locking on the properties of normal modes. With Lognonné et al. (1998) method, all normal modes of the solid Earth-ocean-atmosphere coupled system can be calculated (solid Earth normal modes, acoustic, gravity and lamb atmospheric modes, gravity oceanic modes, i.e. tsunami modes). The eigenfunctions calculated give the distribution of the kinetic and potential energy (Lognonné and Clévédé, 2002), from which the importance coupling between the atmosphere, ocean and solid Earth can be estimated. For the seismic spheroidal normal modes, two regimes are found. Below about 3.7 mHz (the exact frequency depending on the atmospheric model), the atmospheric part of the mode is trapped at the surface and decays exponentially with altitude. At higher frequency, a leakage of seismic energy in the atmosphere is observed, associated to upward acoustic wave propagation (Fig. 2), and about 0.02% of the kinetic energy of the spheroidal fundamental normal modes is transferred to the atmosphere. This leads to the atmospheric signature of surface waves.

The frequencies with maximum coupling are found first near 3.7 mHz, where spheroidal modes have up to 0.05% of their energy in the atmosphere and also near 4.4 mHz. These two maximums result from a wavelength matching of the Rayleigh waves with the mesospheric wave guide and can lead to typical bi-chromatic seismic signals after volcanic atmospheric explosions (e.g. Kanamori et al., 1994; Zürn and Widmer, 1996; Lognonné et al., 1998). Similar effects are observed for the surface waves harmonics (Lognonné and Clévédé, 2002). Fig. 2 shows that the kinetic energy is relatively constant with respect to the altitude for the long period signals: a small focusing in the mesosphere is observed due to the atmospheric trapping and the low frequencies normal modes with $f < 10$ mHz are not strongly affected by the viscous attenuation. Consequently, these modes have an amplitude growing exponentially with the altitude z at the rate of $\exp(z/2H)$, where H is the atmospheric density scale height. Amplitude amplification of 10^6 are, therefore, observed for these long period waves. At higher frequencies, viscous

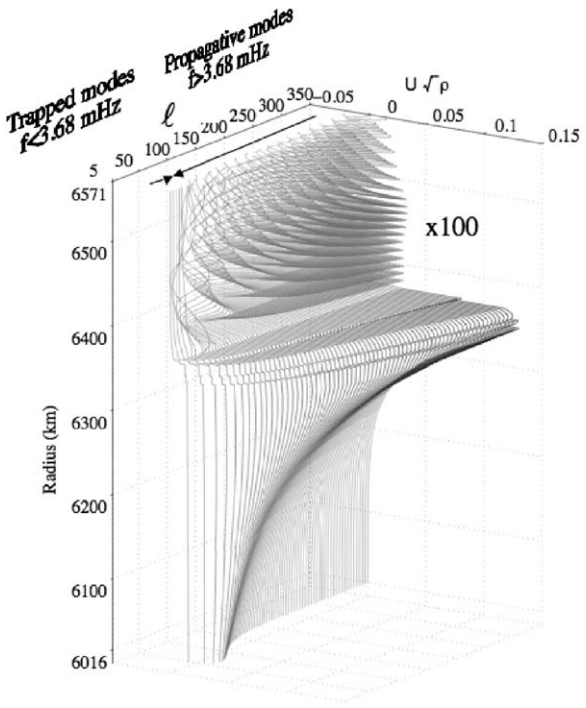

Fig. 2. Amplitude of the solid fundamental ($n = 0$) spheroidal normal modes in the upper mantle and atmosphere, for different angular orders of the modes. Angular orders are related to the horizontal wavelength by the Jean's formula as $\lambda = (2\pi a)/(\ell + 1/2)$, where a is the radius of the Earth and ℓ the angular order. The amplitudes shown are multiplied by the square root of the density and drawn with respect to radius for several normal modes. Amplitudes in the atmosphere are multiplied by 100. A radiative boundary condition is used. PREM model is used for the interior (Dziewonski and Anderson, 1981) and US standard atmospheric model (1976) for the atmosphere.

attenuation is larger and induces a damping of the mode above 150 km of altitude. 30-s period waves reach a peaked amplification of 10^5 at altitude ranging between 200 and 250 km and have then an amplitude decreasing with altitude due to attenuation. GPS observations of seismic signals will be discussed in Section 6.

Tsunami normal modes are also expected to generate inospheric perturbations and a first description of the coupling between tsunami and the atmosphere/ionosphere system was done by Peltier and Hines (1976). The basic reason for their efficient coupling is due to the similar group velocities of the tsunami and of the atmospheric gravity waves (e.g., see Fig. 1 of Lognonné and Clévédé, 2002). This leads to much larger amplitudes of the atmospheric displacement. Fig. 3 shows the example for the tsunami mode with angular order $l = 100$ (at about 40 min of period). We will review in Section 7 the ionospheric tsunami observations and discuss their perspectives.

3. The SPECTRE GPS tomography project

The aim of the Service and Products of ionosphere Electronic Content and Tropospheric Refractive index over

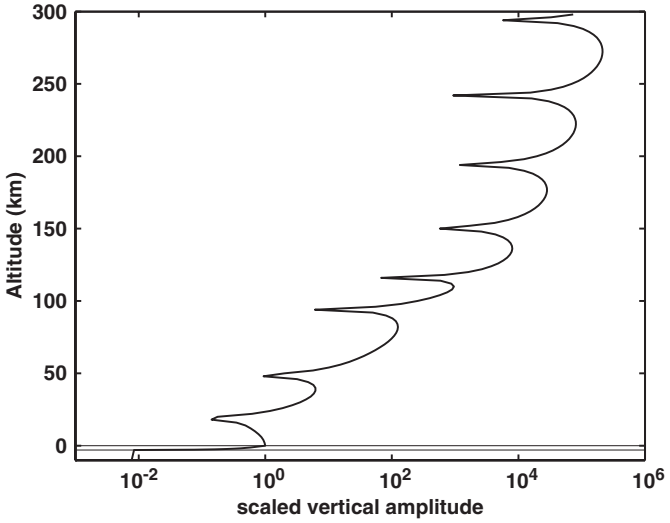

Fig. 3. Vertical amplitude of the tsunami normal mode with angular order $\ell = 100$ and for the PREM earth model (Dziewonski and Anderson, 1981) with 3 km of oceanic water depth and the NRLMSISE-00 (Picone et al., 2002) atmospheric model with local time and location of 2005, December 26 Sumatra event (10°N, 90E, 0H UTC). This angular order corresponds to wavelength and period of about 398 km and 39 min. The amplitude is scaled such it is equal to unity at the sea surface. The boundary condition at the top of the atmosphere is a free surface, which leads to some overestimation in the atmospheric amplitudes.

Europe (SPECTRE) experiment is to perform a 3D monitoring of the ionosphere and troposphere over dense GPS array. We will focus in this paper on the scientific applications of such 3D high resolution models in the detection of post-seismic signals associated to earthquakes and will not detail the other applications of SPECTRE, in term of 3D ionospheric monitoring (for improved performances of GPS mono-frequency receivers or of other ionospheric sensitive systems) or in term of 3D tropospheric monitoring (for meteorological applications).

This post-seismic monitoring will be performed in conjunction with the operation of the CNES Demeter mission (Parrot, 2002). The project is operated by a consortium built between the Institut de Physique du Globe de Paris and the company Noveltis, a French scientific engineering company. The project was initiated during the phase B of Demeter by the IPGP group (Artru, 2001; Ducic, 2004) for the 2D tomography and later developed toward 3D (Garcia et al., 2005). The developed software was then upgraded by the Noveltis team, which has implemented the production web site, located at http://www.noveltis.net/spectre/. Initially limited to Europe, our ionospheric monitoring will be extended to California and Japan during the Demeter mission. The European tomographic models are already available at the Noveltis web site, for the most recent data (current week), and archived data will be available in IPGP when Demeter data will be released.

The used arrays are the European GPS stations from various networks (including EUREF, RGP, REGAL and probably soon, EGNOS), the Japanese GEONET network of about 1300 stations and the Northern (BARD) and Southern (SCIN) Californian networks. Data are freely downloaded from the Internet data servers of these networks. The GPS tomography algorithm, detailed by Artru (2001), Ducic (2004), is based on the measure of propagation times of the GPS modulated carrier signal at two frequencies: f_1 (1575.42 MHz) and f_2 (1227.60 MHz). Tracking the phase difference between the carriers at f_1 and f_2 therefore provides a very precise measure of the dispersion of the signal, which is only due to ionospheric propagation and instrumental biases. For a single receiver, we obtain the propagation time delay between the two GPS signals for frequencies f_1 and f_2 using the geometry-free combination of phase (L_1 and L_2, in cycles) and code (P_1 and P_2, in meters) measurements. The time delay $\tau = t_2 - t_1$ is expressed by

$$\tau = 1/c(\lambda_2 L_2 - \lambda_1 L_1) - 1/c\langle P_2 - P_1 - (\lambda_2 L_2 - \lambda_1 L_1)\rangle, \tag{1}$$

where λ_1 and λ_2 are the wavelengths associated to f_1 and f_2, c is the speed of light in vacuum and $\langle\ \rangle$ represents the mean through any continuous sequence of data for one satellite-receiver couple. This mean allows to determine the ambiguity constant on the phase measurements, related to the unknown number of entire cycles between two consecutives first phase detections of the satellite signals. If N_e is the electronic density, IFB the inter frequency bias associated to the receiver and TGD the transmitter group delay corresponding to the satellite bias (both expressed in time units), we have (Mannucci et al., 1998)

$$\tau(r,s,t) = \mathrm{IFB}(t) + \mathrm{TGD}(t) + \frac{40.3}{c}\left(\frac{1}{f_1^2} - \frac{1}{f_2^2}\right)\int_r^s N_e(x,t)\,\mathrm{d}s, \tag{2}$$

where the integration of the electronic density is done along the radio path between the receiver and the satellite, assumed as straight line in what follows. The basis of the second step, i.e. of the ionospheric tomography procedure, is based on the joint inversion of the ionospheric structure and of all receivers and satellites biases by using the data set of all time delays. The set of unknowns will be called later model and noted **m**. Let us consider the delay τ_i corresponding to a give pair receiver-satellite (i). In the 2D case, we assume that the ionosphere can be reasonably represented as a single layer at an altitude of 350 km, so we can define the vertical total electronic content (VTEC) as the TEC along a vertical profile intersecting the ionosphere at the ionospheric piercing point (IPP). We, therefore, have

$$\int_r^s N_e(u,t)\,\mathrm{d}u = \frac{1}{\cos\theta_i}\,\mathrm{VTEC}(x_i, y_i), \tag{3}$$

where θ_i, x_i, and y_i are the zenithal angle and position of the ionospheric piercing point for the ray associated to the

receiver-satellite pair (i).Noting

$$K = \frac{40.3}{c}\left(\frac{1}{f_1^2} - \frac{1}{f_2^2}\right),$$

we, then, get

$$\tau_i = [\mathbf{Gm}]_i = \begin{bmatrix} \frac{K}{\cos(\theta_i)} & 1 & 1 \end{bmatrix} \times \begin{bmatrix} \mathrm{VTEC}(x_i, y_i) \\ \mathrm{IFB}_i \\ \mathrm{TGD}_i \end{bmatrix}, \quad (4)$$

where $\mathbf{G}$ the model matrix, τ_i the ith component of a vector $\boldsymbol{\tau}$ of the N observed delays and $\mathbf{m}$ a $3 \times N$ model vector. The model vector is defined as the vector with the VTEC values on a given grid plus all IFBs and TGDs. Note, here, that we have chosen to invert also the TGDs values, even if the later are given in the broadcast navigation file. Practically, VTEC values at the IPPs are obtained by linear correlation from the model grid. Due to their time dependence, the time series of models will be inversed by Kalman filtering algorithm. This method allows to set space and time correlation, improving convergence. So the joint inversion involve the minimization for each time step of

$$(\mathbf{Gm} - \tau)^t \mathbf{C}_\mathrm{d}^{-1}(\mathbf{Gm} - \tau) + (m - m_{\mathrm{priori}})^t C_\mathrm{m}^{-1}\left(m - m_{\mathrm{priori}}\right), \quad (5)$$

where C_m and C_d, respectively, are the covariance matrix of the model and of the data and where $\mathbf{m}_{\mathrm{priori}}$ is the a priori model, describing the a priori information on the ionosphere, IFBs and TGDs. If we take no a priori on the IFBs and TGDs, for the ionosphere and the parameter VTEC, we assume that the structures have a typical correlation distance, so that the terms of the covariance matrix are proportional to

$$C_\mathrm{m} \propto \exp^{-\left((x-x')^2+(y-y')^2\right)/D^2}, \quad (6)$$

where x, y, respectively x', y', are the position of two points of the 2D model grid. The covariance matrix is of course scaled by a normalization factor and D is a correlation length of the model grid. C_d is taken as a diagonal matrix (i.e. no correlation is assumed between two GPS stations, even when the same satellite is observed), with a sigma corresponding to 0.1 TEC in noise level.

The result of the inversion is a 2D model of the VTEC, computed as a map, together with the a posteriori map of error. Such maps are provided systematically on the SPECTRE web site. In addition we also obtain from the inversion the satellites and receiver bias. These biases, as well as the set of inverted data (i.e. the TEC values produced by the GPS data, together with the position of the sub ionospheric points) are provided on the web site too.

Ideally, we can produce tomographic maps with the same sampling rate as the original GPS data, i.e. every 30 s. However, a significant aliasing is observed in the 30 s data provided by the GPS networks, as shown by Garcia et al. (2005). Although filtered by the inversion, due to the non-coherency of the aliasing between two different GPS stations, non-aliased maps are therefore produced by the use of a FIR filter, at the cost of a reduced sampling rate of 15 or 60 min. Fig. 4(a) shows typical TEC variations every hour for the date 06/06/2004. Fig. 4(b) plot shows few biases estimations. The field of TEC has been estimated over a 2.5×2.5 degree grid. The prior model for the first iteration is a homogeneous TEC value over the area of interest and initial values for electronic biases have been considered as equal to zero. A correlation length of 10° is used. The convergence of the biases is rapid and the main signatures of the ionosphere dynamics (diurnal variation of the TEC, geomagnetic storms) is well recovered.

As noted earlier and in addition to the study of post-seismic ionospheric signals, the SPECTRE maps can be useful to study phenomena that affect the ionosphere. For example, Fig. 5 shows the correlation between the dynamic of the magnetic field and ionospheric disturbances induced by the extreme magnetic storm of November 2004. One can note the strong correlation between the short period perturbations (<6 h) of the D_{st} index and of the ionosphere for auroral area over Europe (60°N–70°N).

The 3D tomography technique is detailed by Garcia et al. (2005). In the 3D case, we minimize the same expression of Eq. (5) but with a 3D model. The input TEC measurements are filtered in the infrasonic frequency range for seismic monitoring, while no filtering is done for an absolute ionosphere reconstruction. Satellite and station biases variations in this frequency range are neglected. 3D monitoring of the absolute ionospheric electronic content, including biases, will be developed from this first step. 3D SPECTRE models will be progressively be made available during the Demeter project for a final on line release at the end of the mission.

4. Validation

We illustrate the quality of the results by showing resolution tests and a comparison of the TEC estimation with other independent estimates.

To validate the method in the TEC determination, we have compared the TEC estimates from maps generated by the above-described method (in green in Fig. 6) to those deduced from bi-frequency TOPEX altimeter measurements (in red) and DORIS measurements (in blue). We observed a good agreement between the various sources of TEC estimates, with typical differences of 2 TECU. The shift between TOPEX and other estimates is due to a bias coming from the TOPEX inner electronics. In this comparison, the differences of altitude were corrected and the distribution of ionisation with altitude was estimated with IRI model (Bilitza, 1997).

For the resolution, various tests over Europe but also over South California and Japan have been done to validate the TEC algorithms and their resolutions and to confirm that the wavelength of the long period seismic waves (typically 350 km at 100 s) can be recorded in the ionosphere. Fig. 7(a)–(d) show the results of chessboard

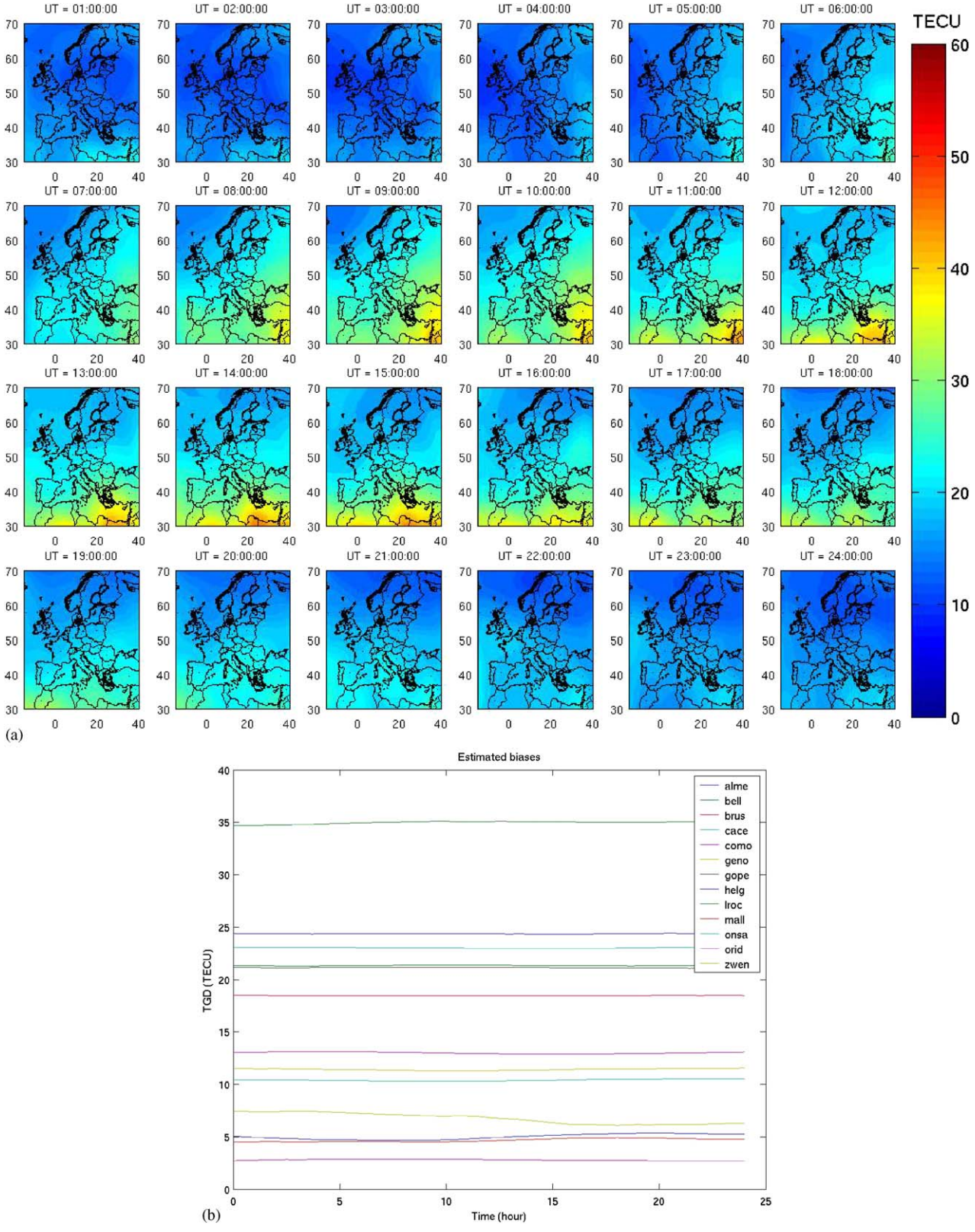

Fig. 4. (a) 1-h TEC maps obtained from dense GPS network over Europe on 06/06/2004. A resolution length of 10° and a a priori noise of 0.1 TECU is used in the inversion, enhancing the large scale structures of the ionosphere. (b) The right bottom figure shows a few of the station bias evolution during the corresponding period.

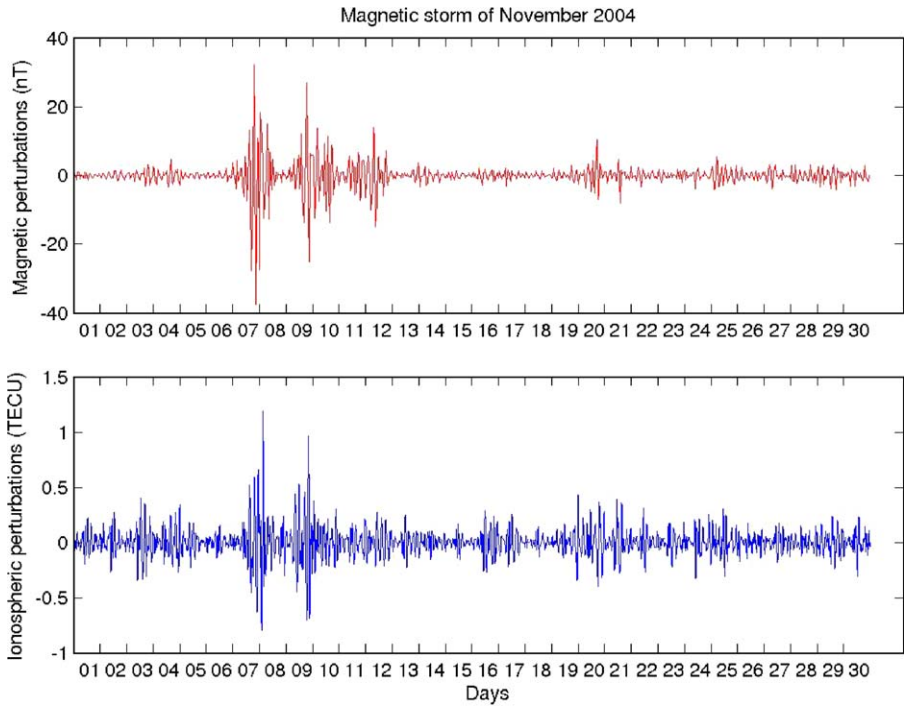

Fig. 5. Top: D_{st} index period low-pass filtered with 6 h period cut-off. Bottom: Mean VTEC in European auroral area (lat $>60^{\circ}$N) filtered with the previous filter.

tests. In these tests, the electronic biases were assumed to be already known and pseudo TEC observations were computed on a grid pattern. Then, for a realistic GPS stations-satellites configuration, the maps were computed. Considering the European network resolution (between 500 and 900 TEC measurements each 30 s), we recover only patterns of wavelength higher than 300 km. Due to the higher resolution of the Japan and South California networks, it is possible to recover finer structures of 50 and 100 km wavelength and good results are, therefore, obtained with correlation length as low as 30–50 km. With larger correlation length, it is also possible to retrieve 2D offshore ionospheric structure in Japan, by using also the low elevation GPS satellites in the inversion. For Europe, larger correlation's length (at least 200 km) must be used and generally, a trade-off must be found between sensitivity and resolution: large correlation length must be used for absolute TEC determinations while smaller ones will reveal small scale TEC variations, with less confidence on the amplitude however.

Similar tests were performed for the 3D resolution. For California and with the Denali Alaska observations in mind (Ducic et al., 2003; Garcia et al., 2005), we have used a synthetic wave structure in the ionosphere propagating from North to South, in order to see how the inversion is able to reconstruct such features. Results are shown on Fig. 8. These last tests show that the horizontal structure of Rayleigh waves is retrieved with the existing networks in California, but also that the resolution is to crude for retrieving the inclination of the wavefront, its amplitude and a detailed picture of the vertical propagation of the ionospheric acoustic waves.

5. GPS detection of seismic waves

GPS networks can image the ionospheric seismic TEC variations every 30 s at high altitude (250–350 km), and in some case at higher rates (1 Hz). Depending on the number of stations, either the 2D ionospheric TEC maps or the 3D ionospheric structure can be reconstructed by the processing. Several signals were observed, either for near field observations, such as those of the Hokkaido (2003) and San Simeon (2003), earthquakes, or in far field, for Rayleigh waves generated by the Alaska, Denali, 2002 event or for the tsunami generated by the Peru, 2001, earthquake. In the case of the Hokkaido event, all waves are observed and a 3D analysis is necessary to separate the waves.

The November 3, 2002 Alaska earthquake ($M_s = 7.9$) gave us the first opportunity to perform such successful remote sensing of Rayleigh waves. A band-pass filter between 150 and 350 s corresponding to a central period of 225 s close to the Airy phase of Rayleigh waves was applied. Data are here plotted as a function of time and epicentral distance, the latter of which changes with time as a result of the satellites orbital motion (Fig. 9(a)). We observed a signal two to three times larger than the noise level, arriving about 660–670 s after the arrival time of Rayleigh waves at the ground. The amplitude of the perturbation varies from satellite to satellite, but the signals

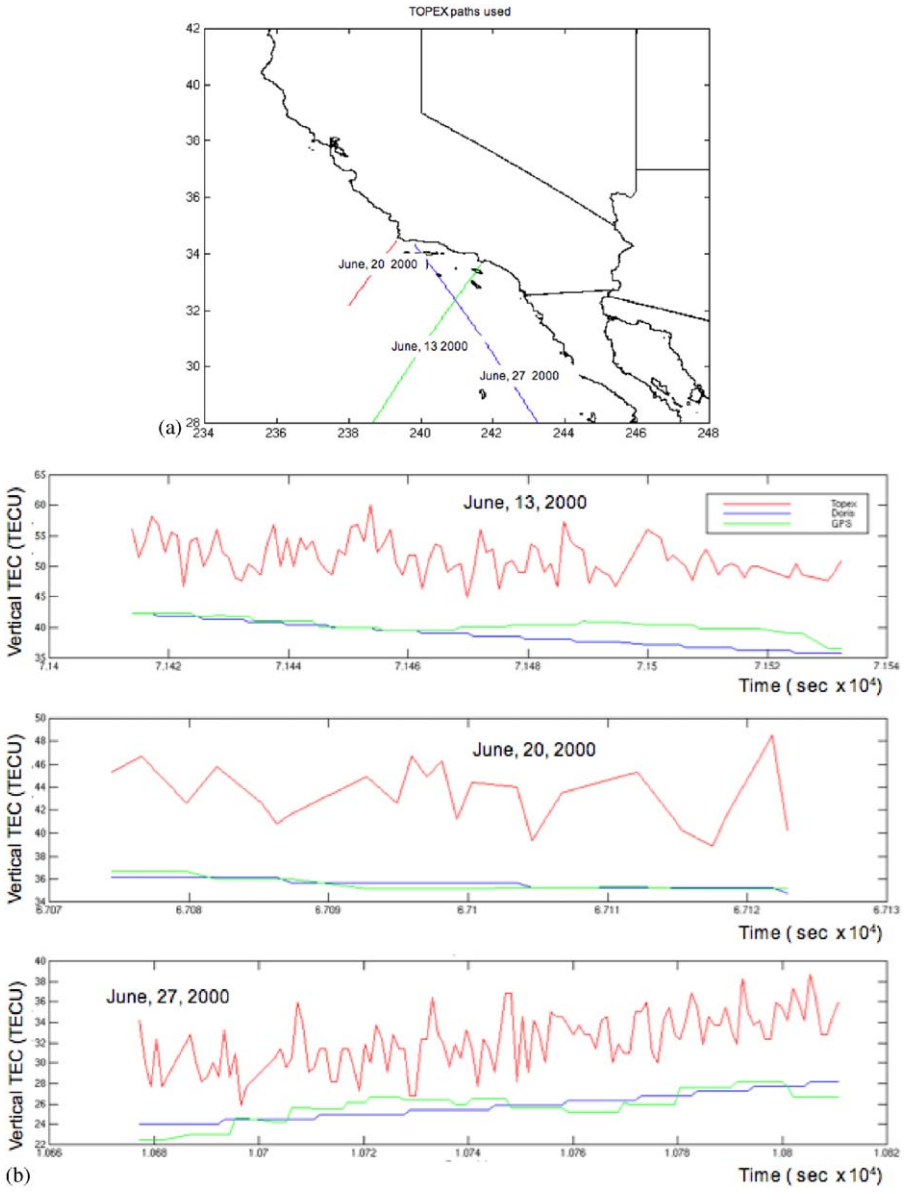

Fig. 6. Comparisons in California between the TEC predicted measurements and DORIS or TOPEX altimeter TEC measurements (three right figures). Red curve is the Topex measurement (including the instrumental bias), blue is the Doris measurement and green the GPS measurement. The corresponding orbits are shown in the right figure.

are consistent and were observed on six others satellites in visibility. The total electron content (about 60 TECU at this local time) is fund to be perturbed by about 0.1% (0.1 TECU peak to peak). Such signals are quite small and it should be noted that the aliasing effects on the 30 s RINEX files is typically 0.01–0.02 TECU (Garcia et al., 2005). We were able to determine, by cross-correlation, the altitude where the signal maximized and to extract from these signals the first group velocity measurement of Rayleigh waves obtained with ground-space measurement techniques, fitting well with the value obtained by tomographic models (Ducic et al., 2003). Further analysis done, with the 3D tomographic analysis of signals (Garcia et al., 2005) have shown that ionospheric perturbation were traveling above the maximum of ionization. Fig. 10 shows the ionospheric waveform, filtered in the frequency bandwidth 4.3, 5.8 mHz for the Denali earthquake. The 1 mm peak-to-peak displacement of the surface is creating a 0.5% electron density perturbation propagating horizontally at ~4 km/s (seismic surface wave velocity) and vertically at ~1.2 km/s (infrasonic sound velocity). Movies of the signal can be downloaded at the following address: http://ganymede.ipgp.jussieu.fr/~garcia/Denali.Vcut.Az2.movie.mpg.gz.

The Hokkaido Tokacho-Oki earthquake of September 25, 2003 gave us another opportunity and spectacular ionospheric waves have been observed. In contrary to the Alaska earthquake observations, these signals are associated to the near-seismic waves and especially to infrasonic waves generated near the source and propagating in

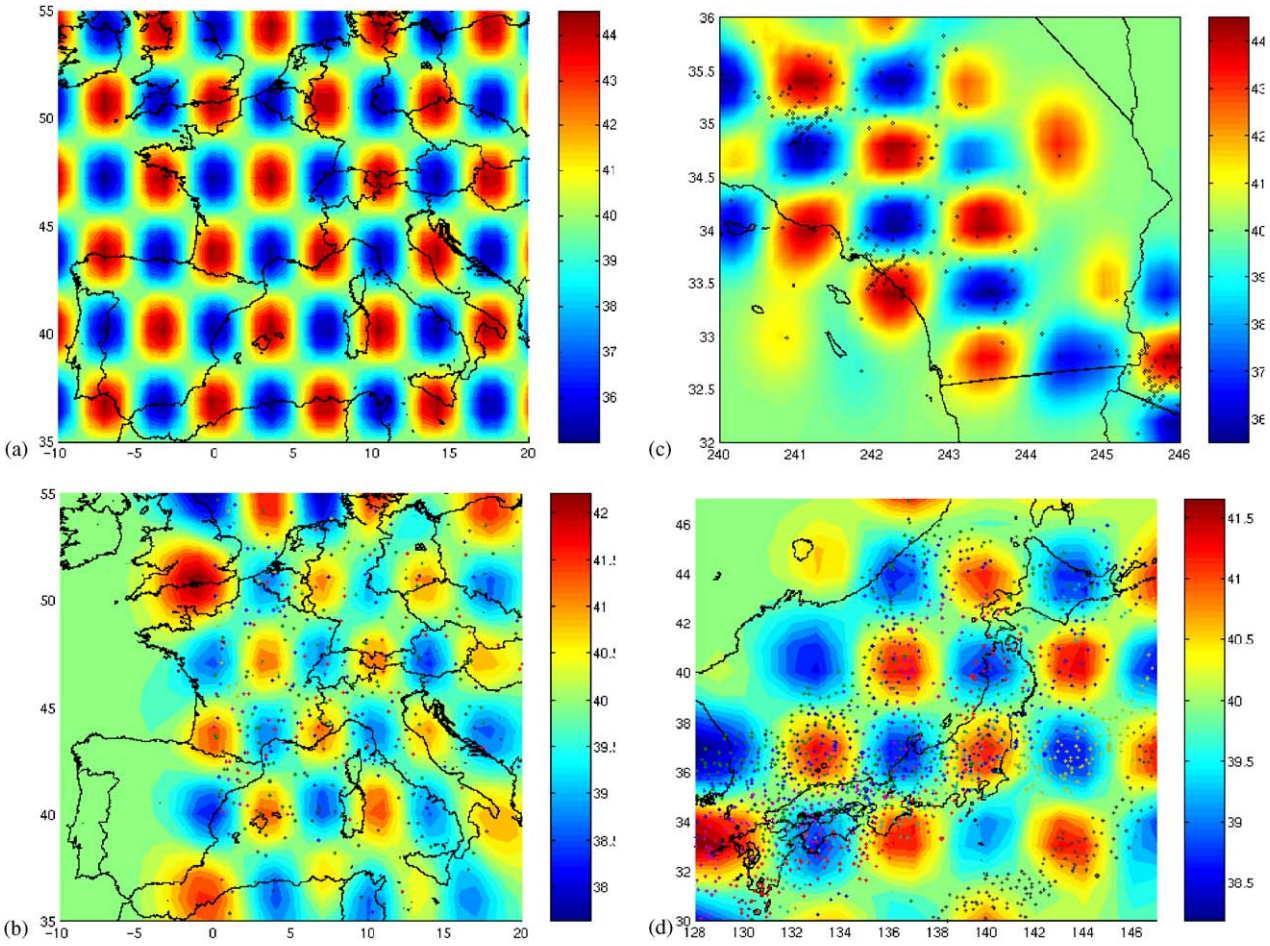

Fig. 7. (a) Input Chessboard for the resolution test for Europe. Units are TEC in TEC units. (b) Output VTEC map for Europe. Points are all the subionospheric piercing points used in the inversion, from a realistic configuration of stations and satellites. The correlation length used was 300 km. (c) Results of the retrieval for South California. The correlation length is 30 km. (d) Results of the retrieval for Japan and for offshore TEC observation. The correlation length in this test is 200 km but as for the California case small-scale features above Japan island are retrieved for correlation length of 30 km.

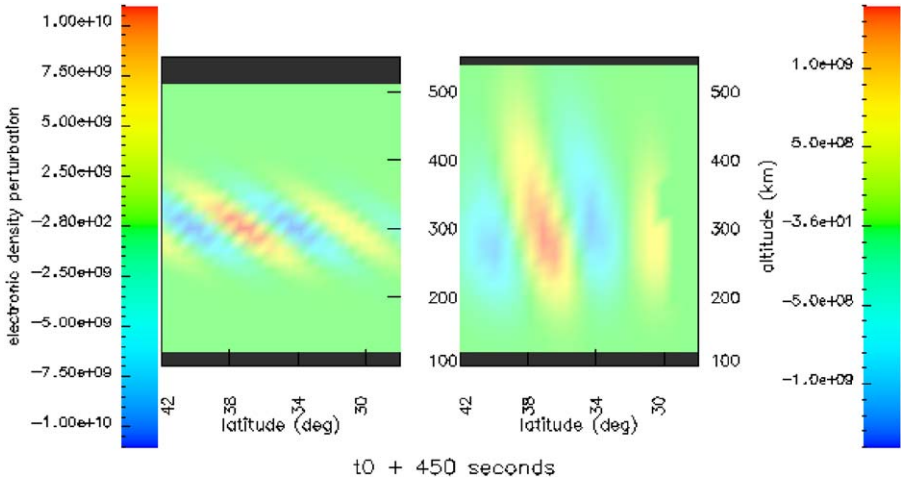

Fig. 8. North–South vertical cut in the Input 3D (left) and in the retrieved 3D (right) wave structures above the California Network.

the atmospheric wave-guide (Fig. 9(b)). These waves are observed up to about 800 km. At further distances, we also observe Rayleigh waves, as for the Denali event. The amplitudes observed are comparable to those of the Denali event and are typically 0.1 TECU peak-to-peak. Fig. 11 shows a series of 2D tomography snapshots, every 30 s. We observe two wavefronts. The first is propagating offshore Hokkaido, while the second one is propagating

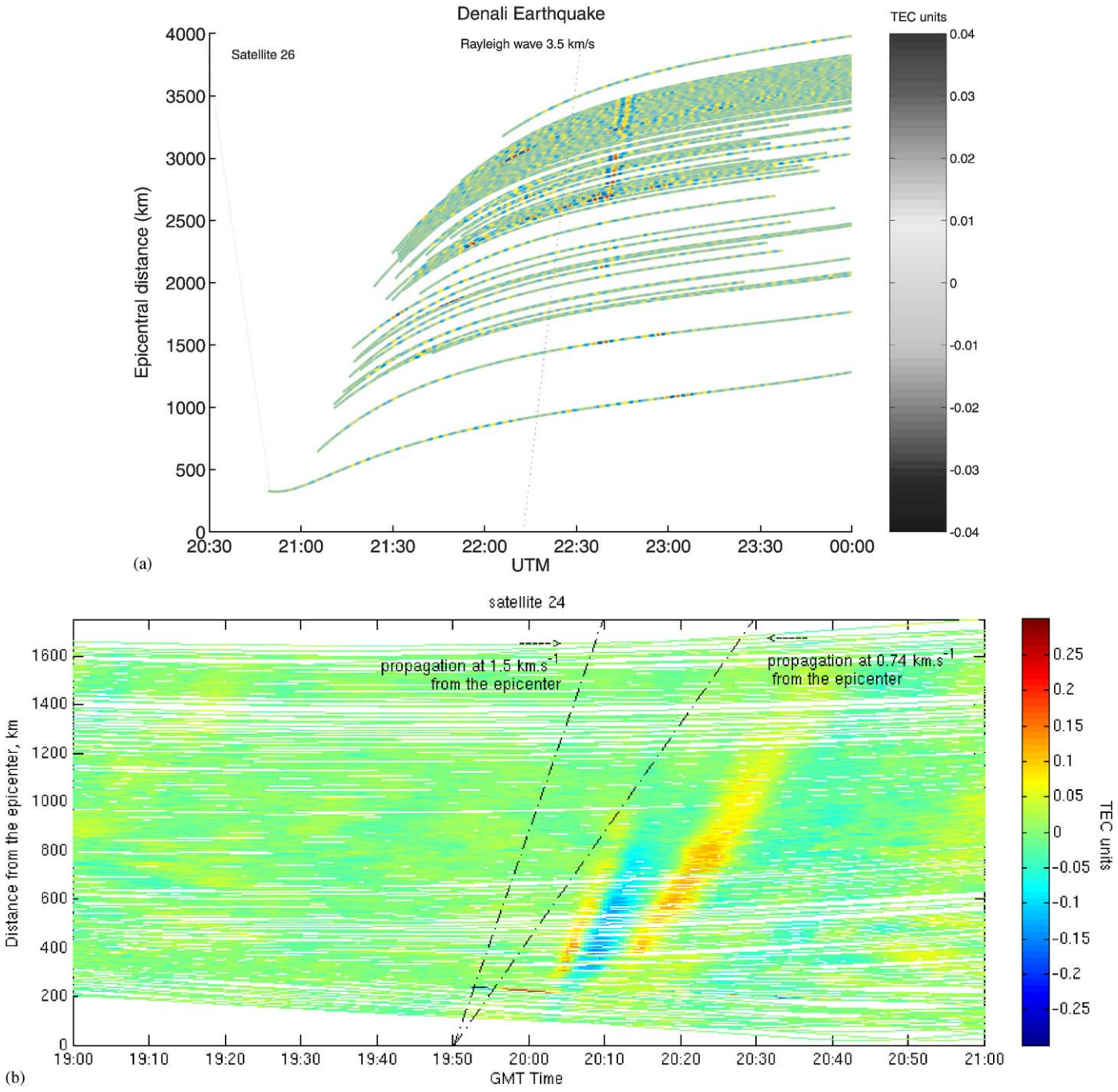

Fig. 9. (a) Left: TEC observation of the Denali Surface waves for the records from satellite 31 of the California Network. Each trace is corresponding to a GPS station and the epicentral distance at a given time is the epicentral distance of the sub-ionospheric point. The black arrow shows the arrival time at the ground while the red arrow shows the arrival time at the maximum of ionization. The Denali earthquake occurred at 22:12:40 GMT. (b) Right: same observation for the Hokkaido earthquake. The observations are done in the near field. We note that the observed velocities in the near field are smaller than Rayleigh waves and that the near field signal, up to about 800 km is mainly an acoustic signal. At 1000 km, the Rayleigh wave signal, despite smaller amplitudes, is also recovered. The Hokkaido earthquake occurred at 19:50:06 GMT.

perpendicular to the Japan's shoreline of the Japan sea. No wavefront is observed with a north or northwest propagation direction. As the coverage of the GPS satellite at the recording time of the event was very poor in these directions, this lack of signal is probably just resulting of a lack of coverage. As this event mix up surfaces waves, acoustic waves and probably also a tsunami, a full analysis of the ionospheric signals will need 3D tomography analysis. Such analysis will be presented in a future paper.

6. Tsunami detections

Tsunami waves propagating across long distances in the open-ocean can induce atmospheric gravity waves by

dynamic coupling at the surface. In the period range 10–20 min, both have very similar horizontal velocities, while the gravity wave propagates obliquely upward with a vertical velocity of the order of 50 m/s, and reaches the ionosphere after a few hours.

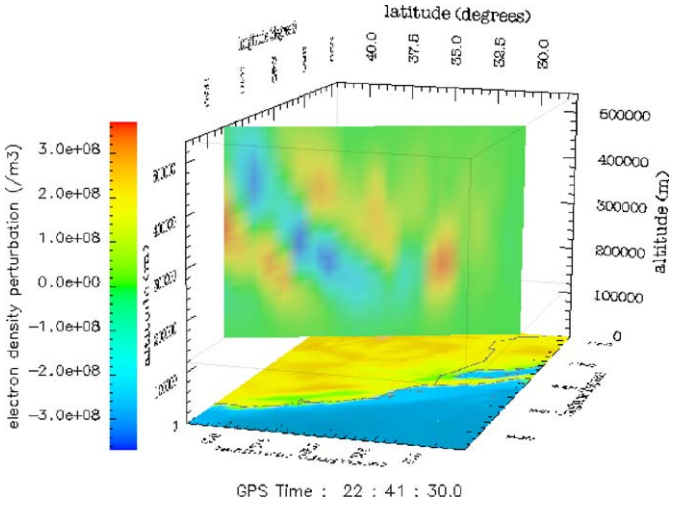

Fig. 10. Retrieved waves for the Denali Earthquake: vertical cut in the 3D model aligned along a direction parallel to the surface waves propagation in a spherical earth.

Even if the possibility to detect the ionospheric signature of tsunami was suggested by Peltier and Hines (1976), the first detection of tsunami in the ionosphere, reported by Artru et al. (2005) was done 30 years after. The above-described ionospheric GPS monitoring was used to image a perturbation possibly associated with a tsunami-gravity wave. The tsunami was produced after the $M_w = 8.2$ earthquake in Peru on June 23, 2001 with run-up reaching locally 2–5 m. The tsunami propagated across the Pacific Ocean and was detected on tide gauge measurements along the coast of Japan (International Tsunami Information Center 2001) with amplitudes between 10 and 40 cm, 20–22 h after the earthquake. Numerical simulation predicted a first peak arrival there approximately 21–23 h after the event (i.e. 17:30–19:30 GMT on June 24), with open-ocean amplitudes between 1 and 2 cm in the Northern Pacific and a short-scale ionospheric perturbation presenting the expected characteristics of a coupled tsunami-gravity wave (Fig. 12) was detected around that time.

The gigantic and dramatic Sumatra tsunami of December 26, 2004 ($M = 9$, 00:58 UTC) confirmed the

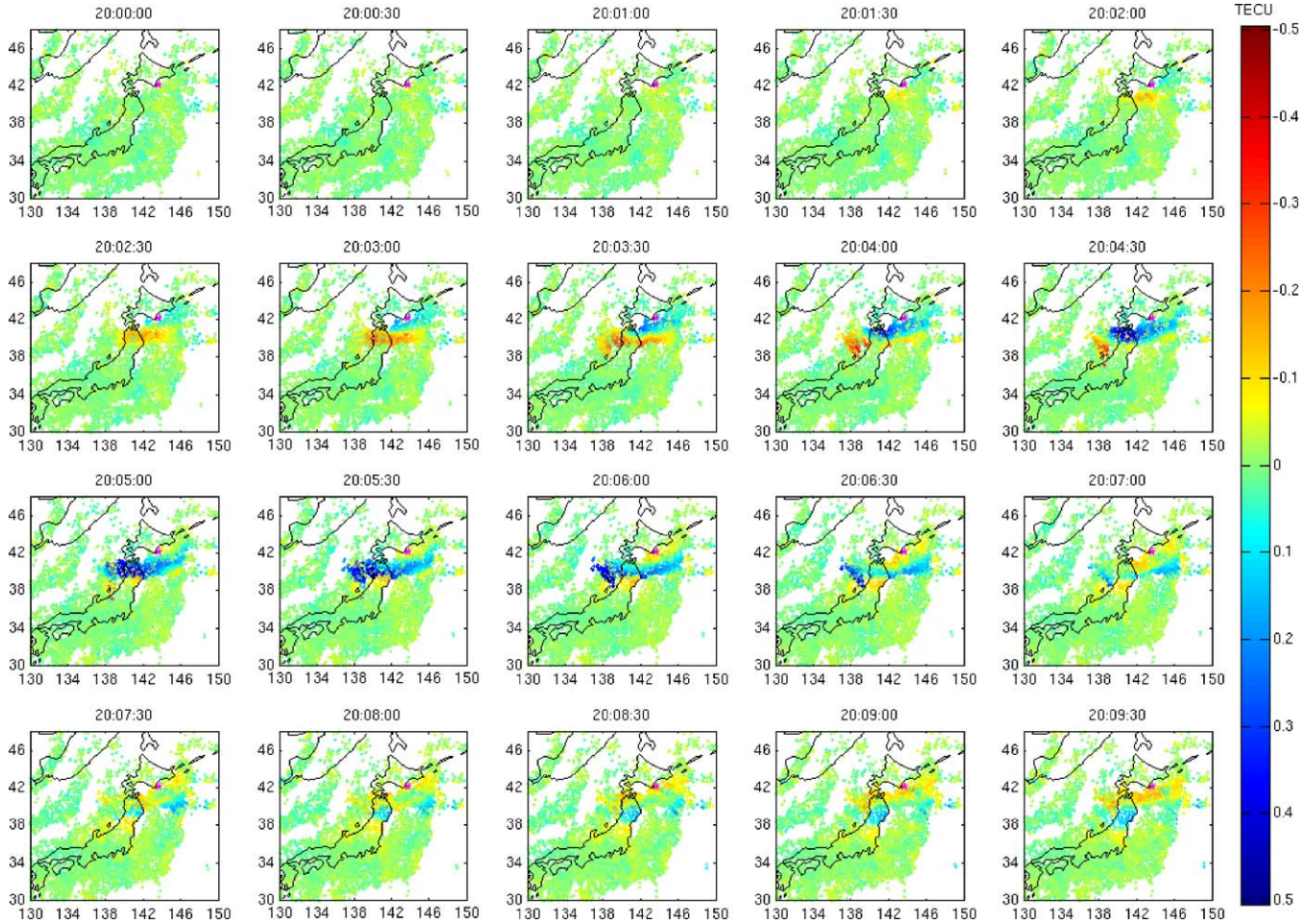

Fig. 11. Map of the ionospheric perturbations over Japan after the Hokkaido earthquake. Each map is performed every 30 s. A spectacular ionospheric perturbation is observed, corresponding mainly to acoustic waves generated by the quake and appears approximately 10 min after. The earthquake occurred at 19h50 UT while the first map is at 20h00 UT.

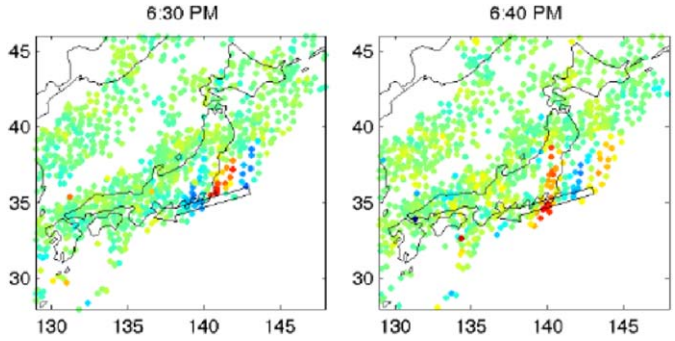

Fig. 12. Observed signal: TEC variations plotted at the ionospheric piercing points. A wave-like disturbance is propagating towards the coast of Honshu. This perturbation presents the expected characteristics of a tsunami-induced gravity waves, and arrives approximately at the same time as the tsunami wave itself. Peak to peak amplitudes are about 1 TECU.

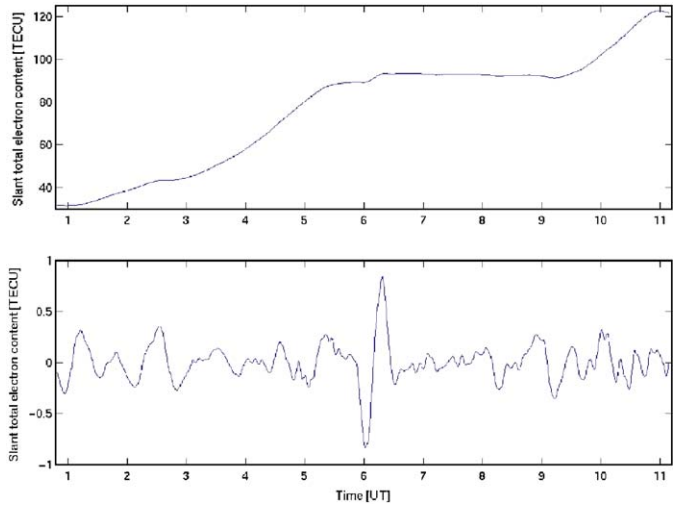

Fig. 13. Ionospheric perturbation observed at the DGAR/IGS station from GPS satellite 28. The sub-ionospheric point is approximately located at 1.65N and 72.78E for an altitude of 350 km, at an epicentral distance of 2460 km of the tsunami. The top trace is the Slant Total Electronic content, while the bottom trace is filtered between .3 and 3.3 mHz.

possibilities of observing tsunami ionospheric signals and several IGS GPS stations detected large ionospheric signals (Fig. 13). Comparable ionospheric signals were also found on other GPS stations (Vigny et al., 2005; Liu, 2005) and on the TEC measurement on-board TOPEX/Poseidon and JASON, with very large TEC signals well correlated to the vertical oceanic displacement (Lognonné et al., 2005b), but the lack of network measurements makes measurement of the azimuth and velocity of the perturbations impossible. In all cases, the ionospheric perturbations are observed about 1 h after the tsunami arrival at the ocean surface. TEC perturbations associated to tsunami will therefore be searched in the future Demeter's and GPS's observations.

7. Perspectives

These ionospheric TEC monitoring of Europe, California and Japan can be used for several scientific investigations, in addition to the study of post-seismic signals. The expected long TEC monitoring will be first used to search for possible TEC anomalies before earthquakes in these regions (Pulinets et al., 2003). TEC anomalies have indeed been already reported. Zaslavski et al. (1998), by using the Topex TEC data, have monitored atypical variations up to 48 h before earthquakes and claim that such variations are found in 34% of the case, instead of 16% for a purely random list of events. Large TEC reductions were also found a few days before the Chi–Chi earthquake (Liu et al., 2001). Naaman et al. (2001) performed however another study for earthquakes in Japan, California and Israel and found no detectable TEC disturbances caused by right-lateral strike-slip earthquakes with minor vertical displacement. We expect to continue such studies, with both the SPECTRE and the Demeter data, with a new search for possible anomalies in Japan, California and Europe before quakes occurring during the Demeter mission and to determine statistically if any correlation between these anomalies and quakes can be demonstrated.

The other perspectives will be to increase observations and interpretations of post-seismic signals. More observations of these signals will open new applications. The first will be related to the early warning of tsunami, in addition with other tsunami warning techniques. Other will be found in tomographic studies of the lithosphere with surface waves. While the ionosphere is an amplifier for the detection of surface waves, it is indeed not affecting the horizontal propagation of these waves, which depend on the lithospheric seismic velocities at a depth depending on their frequency (about 100 km for 100 s waves). The determination of the horizontal propagation velocity of the seismic waves can therefore be helpful for lithospheric tomographic studies, especially in Earth's area without dense broadband seismic networks, such as oceans.

Acknowledgment

This works was funded by the French Ministry of Research (RTE SPECTRE), by ESA under a Space weather pilot project activity and by CNES. We thank CEA/DASE, the GSI-GEONET Japan GPS network, the California GPS Networks (SCIGN + BARD + IGS) and the European GPS networks for providing us with the data. We thank V. Bazin, G. Auffray and S. Saillant from ONERA Nostradamus team for fruitful discussions and two anonymous reviewers for constructive comments. This is IPGP contribution 2079.

References

Afraimovich, E.L., Palamartchouk, K.S., Perevalova, N.P., 1998. GPS radio interferometry of travelling ionospheric disturbances. J. Atmosph. Solar Terr. Phys. 60, 1205–1223.

Afraimovich, E.L., Kosogorov, E.A., Perevalova, N.P., Plotnikov, A.V., 2001a. The use of GPS arrays in detecting shock-acoustic waves generated during rocket launching. J. Atmosph. Solar Terr. Phys. 63, 1941–1957.

Afraimovich, E.L., Perevalova, N.P., Plotnikov, A.V., Uralov, A.M., 2001b. The shock-acoustic waves generated by the earthquakes. Ann. Geophys. 19, 395–409.

Artru, J., 2001. Ground-based or satellite observations and modeling of post-seismic ionospheric signals. Ph.D., Institut de Physique du Globe de Paris (in French), http://ganymede.ipgp.jussieu.fr/These_JA.pdf

Artru, J., Lognonné, P., et Blanc, E., 2001. Normal modes modeling of post-seismic ionospheric oscillations. Geophys. Res. Lett. 28, 697–700.

Artru, J., Farges, T., Lognonné, P., 2004. Acoustic waves generated from seismic surface waves: propagation properties determined from Doppler sounding observation and normal-modes modeling. Geophys. J. Int. 158, 1067–1077.

Artru, J., Ducic, V., Kanamori, H., Lognonné, P., Murakami, M., 2005. Ionospheric detection of gravity waves induced by tsunamis. Geophy. J. Int. 160, 840–848.

Bilitza, D., 1997. International reference ionosphere—status 1995/96. Adv. Space Res. 20, 1751–1754.

Blanc, E., 1985. Observations in the upper atmosphere of infrasonic waves from natural or artificial sources: A summary. Ann. Geophys. 3 (6), 673–688.

Bolt, B.A., 1964. Seismic air waves from the great Alaska earthquake. Nature 202, 1095–1096.

Calais, E., Minster, J.B., 1995. GPS detection of ionospheric perturbations following the January 17, 1994, Northridge earthquake. Geophys. Res. Lett. 22, 1045–1048.

Calais, E., Minster, J.B., 1996. GPS detection of ionospheric perturbations following a Space Shuttle ascent. Geophys. Res. Lett. 23, 1897–1900.

Calais, E., Minster, J.B., Hofton, M.A., Hedlin, M.A.H., 1998a. Ionospheric signature of surface mine blasts from global positioning system measurements. Geophys. J. Int. 132, 191–202.

Calais, E., Minster, J.B., Bernard, J., 1998b. GPS, Earthquake, the ionosphere and Space Shuttle. Phys. Earth Planet 105, 167–181.

Calais, E., Haase, J.S., Minster, J.B., 2003. Detection of ionospheric perturbations using a dense GPS array in Southern California. Geophys. Res. Lett. 30, 30–31.

Davies, J.B., Archambeau, C.B., 1998. Modeling of atmospheric and ionospheric disturbances from shallow seismic sources. Phys. Earth Planet. Inter. 105, 183–199.

Davies, K., Baker, D.M., 1965. Ionospheric effects observed around the time of the Alaskan earthquake of March 28, 1964. J. Geophys. Res. 70, 1251–1253.

Ducic,V., 2004. Tomographie de l'ionosphère et de la troposphère à partir de données GPS denses. Applications aux risques naturels et amélioration de l'interférométrie SAR. Ph. D., Institut de Physique du Globe de Paris (in french), http://www.ipgp.jussieu.fr/inst/publis/THESES/20040304.pdf

Ducic, V., Artru, J., Lognonné, P., 2003. Ionospheric remote sensing of the Denali Earthquake Rayleigh surface waves. Geophys. Res. Lett. 30 (18), 1951.

Dziewonski, A., Anderson, D.L., 1981. Preliminary reference Earth model. Phys. Earth Planet. Inter. 25, 297–356.

Garcia, R., Crespon, F., Ducic, V., Lognonné, P., 2005. 3D ionospheric tomography of post-seismic perturbations produced by the Denali earthquake from GPS data. Geophys. J. Int. 163, 1049–1064, doi:10.1111/j.1365-246X.2005.02775.X.

Hines, C.O., 1960. Internal atmospheric gravity waves. Can. J. Phys. 38, 1441–1481.

Kanamori, H., Mori, J., Harkrider, D.G., 1994. Excitation of atmospheric oscillations by volcanic eruptions. J. Geophys. Res. 22, 21947–21961.

Li, Y.Q., Jacobson, A.R., Carlos, R.C., Massey, R.S., Taranenko, Y.N., Wu, G., 1994. The blast wave of the Shuttle plume at ionospheric heights. Geophys. Res. Lett. 21, 2737–2740.

Liu, J.Y., 2005. Iononami–ionospheric tsunami signature. In: Second AOGS 2005 Annual Meeting, Abstract 58-SE-A1290.

Liu, J.Y., Chen, Y.I., Chuo, Y.J., Tsai, H.F., 2001. Variations of ionospheric total electron content during the Chi-Chi earthquake. Geophys. Res. Lett. 28, 1383–1386.

Lognonné, P., Clévédé, E., 2002. Chapter 10: normal modes of the earth and planets. In: Kanamori, H., Jennings, P., Lee, W. (Eds.), Handbook on Earthquake and Engineering Seismology. IASPEI Centennial Publications, International Geophysics series, 81A, Academic, New York.

Lognonné, P., Clévédé, C., Kanamori, H., 1998. Normal mode summation of seismograms and barograms in an spherical Earth with realistic atmosphere. Geophys. J. Int. 135, 388–406.

Lognonné, P., Jeansou, E., Garcia, R., Artru, J., Occhipinti, G., Crespon, F., Achache, J., Helbert, J., Moreaux, G., 2005. Detection of the Ionospheric perturbation associated to the tsunami of December 26, 2004 with Topex and Jason-1 TEC data. Geophysical Research Abstracts, Vol. 7.

Mannucci, A.J., Wilson, B.D., Yuan, D.N., Ho, C.H., Lindqwister, U.J., Runge, T.F., 1998. A global mapping technique for GPS-derived ionospheric electron content measurements. Radio Sci. 33, 565–582.

Naaman, Sh., Alperovich, L.S., Wdowinski, Sh., Hayakawa, M., Calais, E., 2001. Comparison of simultaneous variations of the ionospheric total electron content and geomagnetic field associated with strong earthquakes. Nat. Hazards Earth Syst. Sci. 1, 53–59.

Parrot, M., 2002. The micro-satellite DEMETER. J. Geodyn. 33, 535–541.

Parrot, M., Achache, J., Berthelier, J.J., Blanc, E., Deschamps, A., Lefeuvre, F., Menvielle, M., Plantet, J.L., Tarits, P., Villain, J.P., 1993. High-frequency seismo-electromagnetic effect. Phys. Earth Planet Int. 77, 65–83.

Peltier, W.R., Hines, C.O., 1976. On the possible detection of tsunamis by a monitoring of the ionosphere. J. Geophys. Res. 81 (12), 1995–2000.

Picone, J.M., Hedin, A.E., Drob, D.P., Aikin, A.C., 2002. NRLMSISE-00 empirical model of the atmosphere: Statistical comparisons and scientific issues. J. Geophys. Res. 107 (A12), 1468.

Pulinets, S.A., Legen'ka, A.D., Gaivoronskaya, T.V., Depuev, V.Kh., 2003. Main phenomenological features of ionospheric precursors of strong earthquakes. J. Atmosph. Solar Terr. Phys. 65, 1337–1347.

Tsai, H.F., Liu, J.Y., 1999. Ionospheric total electron content response to solar eclipses. J. Geophys. Res. 104, 12657–12668.

US Standard atmosphere model, 1976. Committee on the extension to the standard atmosphere. US Goverment printing office, Washington DC.

Vigny, C., Simons, W.J.F., Abu, S., Bamphenyu, R., Satirapod, C., Hashizume, M., Subarya, C., Tregoning, P., Ambrosius, B.A.C., 2005. Monitoring of the December 26th mega-thrust earthquake in SE-ASIA by GPS. Geophysical Research Abstracts, 7, EGU05-A-10732.

Weaver, P.F., Yuen, P.C., Prolss, G.W., Furumoto, A.S., 1970. Acoustic coupling in the ionosphere from seismic waves of the earthquake at Kurile Islands on August 11, 1969. Nature 226, 1239–1241.

Wolcott, J.H., Simons, D.J., Lee, D.D., Nelson, R.A., 1984. Observation of an ionospheric perturbation arising from the Coalinga earthquake of May 2. J. Geophys. Res. 89, 6835–6839.

Yuen, P.C., Weaver, P.F., Suzuki, R.K., Furumoto, A.S., 1969. Continuous traveling coupling between seismic waves and the ionosphere evident in May 1968 Japan earthquake data. J. Geophys. Res. 74, 2256–2264.

Zaslavski, Y., Parrot, M., Blanc, E., 1998. Analysis of TEC measurements above active seismic regions. Phys. Earth Planet. Int. 105, 219–228.

Zürn, W., Widmer, R., 1996. World wide observation of bichromatic long-period Rayleigh-waves excited during the June 15, 1991 Eruption of Mt. Pinatubo. In: Newhall, C., Punongbayan, R. (Ed.), Fire and Mud, Eruptions of Mount Pinatubo, Philippines. Philippin Institute of Volcanology and Seismology, Quezo City and University of Washington Press, pp. 615–624.